Search for narrow structures in $\bar{p}p$ total cross section from 395 to 740 MeV/c

K. Nakamura, H. Aihara, J. Chiba, H. Fujii, T. Fujii, H. Iwasaki,* T. Kamae, T. Sumiyoshi,* Y. Takada,† T. Takeda, and M. Yamauchi
Department of Physics, University of Tokyo, Tokyo 113, Japan

H. Fukuma* and T. Takeshita‡
Department of Physics, Hiroshima University, Hiroshima 730, Japan
(Received 17 August 1983)

We report the final results of a search for narrow structures in the $\bar{p}p$ total cross section between 395 and 740 MeV/c with a rms mass resolution of 1.5 MeV around the S-resonance region. A reanalysis of the data significantly improved the statistical accuracy. No evidence is found for narrow structures and a 90%-confidence-level upper limit of 24 mb MeV is set at around 500 MeV/c for the integrated cross section of a Breit-Wigner-type resonance of width $\lesssim 4$ MeV.

I. INTRODUCTION

In recent years, considerable experimental efforts have been made in search of baryonium states. Although several candidate states have been reported in the $\bar{p}p$ system, they all have failed to be confirmed in subsequent higher-statistics experiments,[1] except a few very recent observations.[2]

Among the reported baryonium candidates, the S resonance ($\sim$1936) has a peculiar history. It was first observed by Carroll *et al.*[3] as a peak in $\bar{p}p$ and $\bar{p}d$ total cross sections. The narrow width of this peak (less than 10 MeV) stimulated further experimental investigation, and several groups reported its confirmation in $\bar{p}p$ formation experiments.[4–6] However, the characteristics of the S resonance determined from these positive experimental results did not seem to be in good agreement with each other (see Table I). It was also puzzling that the S-resonance signal was not observed in the charge-exchange channel,[7] in spite of its appearance in the elastic channel.

At that time, these limitations were not taken very seriously, and the existence of the narrow S resonance seemed to be almost established. However, this optimistic view was soon turned over by the subsequent $\bar{p}p$ formation experiments[8–12] in which no evidence was found for the narrow S resonance. Meanwhile, Allen *et al.*[13] reanalyzed the bubble-chamber film used by Chaloupka *et al.*[4] and concluded with higher statistics that the previously reported enhancement at 1936 MeV had been caused by a combined effect of a certain instrumental bias and an inadequate analysis.

Observation of a narrow $\bar{p}p$ peak in the S region was also reported in a few production experiments. Daum *et al.*[14] observed a 4σ peak in the reaction $pp \to (\bar{p}p)X$ at 93 GeV, and Aston *et al.*[15] reported a 4.5σ peak in a photoproduction experiment $\gamma p \to (\bar{p}p)X$ at 44—70 GeV. However, Daum *et al.*[16] could not confirm the existence of this peak in the reaction $pBe \to (\bar{p}p)X$ at 100 GeV with

TABLE I. The parameters of the S resonance reported in $\bar{p}p$ formation experiments. p is laboratory beam momentum, M_R is mass, Γ is width, and σ_R is total resonance cross section.

Authors	p (MeV/c)	M_R (MeV)	Γ (MeV)	σ_R (mb)	$\Gamma\sigma_R$ (mb MeV)	Mass resolution at $\sim$500 MeV/c (MeV)
Carroll *et al.*[a]	475	1932 ±2	9^{+4}_{-3}	18^{+6}_{-3}	162±25	4 (rms)
Chaloupka *et al.*[b]	491	1935.9±1	$8.8^{+4.3}_{-3.2}$	10.6±2.4	93±21	1.5 (rms)
Brückner *et al.*[c]	505	1939 ±3	≤ 4	12.5±3	50±15[g]	4 (FWHM)
Sakamoto *et al.*[d]	489	1935.5±1	2.8±1.4	14.5±3.9	41±11	
Hamilton *et al.*[e]	505	1939 ±2	22±6	3.0±0.7	66±24	1.5 (rms)
Amsler *et al.*[f]	491	1936	4			0.4 (rms)

[a]Reference 3.
[b]Reference 4.
[c]Reference 5.
[d]Reference 6.
[e]Reference 8.
[f]Reference 17.
[g]Taken from Ref. 18.

much improved statistics than their previous experiment.[14]

Although the narrow S resonance was not confirmed, Hamilton *et al.*[8] instead suggested possible existence of a wider enhancement (width ~ 20 MeV) in the S region in both total and annihilation cross sections of the $\bar{p}p$ interactions. This structure, again, was not confirmed by subsequent high-statistics measurement of the $\bar{p}p$ total cross section by Sumiyoshi *et al.*[12]

The issue of the narrow S resonance, however, has been raised again very recently. Amsler *et al.*[17] have measured the $\bar{p}p$ annihilation cross section with good mass resolution, and have observed a narrow structure (width ~ 4 MeV) at 1936 MeV. They point out that the structure observed in their previous experiment (Brückner *et al.*[5]) is essentially reproduced.

We summarize in Table I the characteristics of the S resonance reported in formation experiments with positive results. A summary of the negative results is given in Table II. Probably, there is now consensus among various experimental results that the existence of the original S resonance claimed by Carroll *et al.*,[3] having an integrated cross section of 160 mb MeV, has been clearly rejected. However, as we have seen above, there still remains a debate on whether the narrower and smaller S resonance exists or not, and further information is clearly needed.

In view of this, we report the result of $\bar{p}p$ total cross section measurement at beam momenta between 396 and 737 MeV/c with a rms mass resolution of 1.5 MeV at around 500 MeV/c. This result is obtained from a reanalysis of the data reported in our previous publication.[9] Based on the experience gained in our later $\bar{p}p$ experiment,[12] it has become clear that some restrictive requirements imposed on the data in the previous analysis[9] can be safely dropped. (Details will be discussed in Sec. III A.) This significantly improved the statistical accuracy of the result and enabled us to test the existence of a narrow resonance having an integrated cross section down to ~ 20 mb MeV. Also the absolute values of total cross section, which were about 6% lower in our previous results[9] than the "world average" values, have now become consistent with other data.

II. DESCRIPTION OF EXPERIMENT

A. General

In this experiment, the total cross section was measured based on a transmission method. Our technique, however, is distinguished from that of a *conventional* transmission-counter experiment equipped with a series of concentric circular scintillation counters in the following points:

(i) A beam-monitoring spectrometer was equipped.

(ii) The trajectories of the incident-beam particle and the transmitted particle were determined by multiwire proportional chambers (MWPC's) in each event.

(iii) Also pulse-height and time-of-flight (TOF) information from trigger counters and from transmission counters was recorded in each event.

We adopted this technique since it was believed to be particularly suited for a search for narrow resonances in the total cross section of the low-momentum $\bar{p}p$ interactions, which are characterized by a steeply falling total cross section and a large probability of annihilation reactions. Here, stability of the beam is of key importance so as not to produce any spurious structure due to the fluctuation of the momentum and phase space of the beam. Stability of the photomultiplier gains is another important factor. In this experiment, these are continuously monitored during the measurement. On the other hand, the *conventional* transmission-counter experiment is essentially an experiment with counters and scalers only, where high statistics are easily accomplished but the beam properties and photomultiplier gains are only intermittently calibrated and monitored.

An additional advantage of our technique consists in the fact that the differential cross section of forward elastic scattering is automatically obtained.[19,20] This means that the real-to-imaginary ratio of the forward amplitude can be determined, at least in principle, consistently with the total cross section.

B. Apparatus

The experiment was carried out in a low-momentum separated beam line, K3, at the National Laboratory for

TABLE II. Summary of the $\bar{p}p$ formation experiments in which no evidence was found for the S resonance. σ_{ann} and σ_{tot} are the annihilation cross section and total cross section, respectively.

Authors	Measured quantity	Mass resolution at ~ 500 MeV/c (MeV)	Upper limit at ~ 500 MeV/c (mb MeV)
Jastrzembski *et al.*[a]	σ_{ann}	± 1.5	12 (90% C.L. for $\Gamma \lesssim 4$ MeV)
Lowenstein *et al.*[b]	σ_{ann}	2.5 (rms)	16 (2σ for $\Gamma \lesssim 4$ MeV)
Kamae *et al.*[c]	σ_{tot}	1.5 (rms)	40 (90% C.L. for $\Gamma = 3$ MeV)
Allen *et al.*[d]	σ_{tot}	2 (FWHM)	
Sumiyoshi *et al.*[e]	σ_{tot}	3 (rms)	10 (90% C.L. for $\Gamma \geq 10$ MeV)
Present result	σ_{tot}	1.5 (rms)	24 (90% C.L. for $\Gamma \lesssim 4$ MeV)

[a]Reference 10.
[b]Reference 11.
[c]Reference 9.
[d]Reference 13.
[e]Reference 12.

High Energy Physics (KEK). The K3 line was operated in high-resolution mode (L-mode). The intensity of the antiproton beam was 100 $\bar{p}$ at 500 MeV/c per 10^{12} primary protons of 12 GeV/c impinging on a 40-mm-long platinum target, increasing to 700 $\bar{p}$ at 700 MeV/c. The $\pi^-/\bar{p}$ ratio was about 300 at 500 MeV/c, decreasing to 130 at 700 MeV/c. The momentum bite transmitted was $\pm 2\%$.

Figure 1 shows a plan view of the beam line and the experimental apparatus. The momentum of each beam particle was measured by a scintillation-counter hodoscope $H1$ located at a momentum-dispersive focus of the K3 line, where the momentum dispersion was 2.8 cm/(1% $\Delta p/p$). The hodoscope $H1$ had thirty-six 5-mm-wide and 3-mm-thick elements.

We used a liquid-hydrogen target with a double-cylinder structure. The outer cylinder, made of stainless steel, was 80 mm long and 74 mm in diameter with 250-μm-thick Mylar windows at both ends. The concentric inner cylinder with 65-mm diameter was made of thin aluminum. This structure reduced the density fluctuation due to bubbling of liquid hydrogen inside the inner cylinder,[21] since bubbles were mostly created on the surface of the outer cylinder and were guided to a gas outlet line through the space between the inner and outer cylinders. The length of the liquid-hydrogen target along the cylinder axis was 86.5 mm under the operating condition (20.4 K, 1 atm). An empty target had the same structure as the liquid-hydrogen target. They were installed

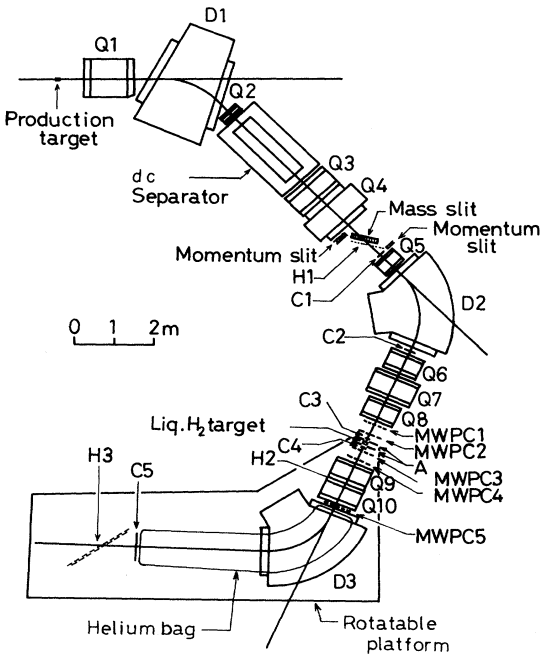

FIG. 1. Plan view of the experimental apparatus. $D1$—$D3$, bending magnets; $Q1$—$Q10$, quadrupole magnets; $C1$—$C5$ and A, scintillation counters; $H1$—$H3$, scintillation-counter hodoscopes; and MWPC1—MWPC5, multiwire proportional chambers.

TABLE III. Summary of the trigger and transmission counters. They were all viewed by RCA 8575 photomultipliers. The plastic scintillator used was NE104.

Counter	Width (mm)	Height (mm)	Thickness (mm)	No. of photomultipliers
C1	120	40	3	2
C2	210	60	1	2
C3	40 (diam)		1	2
C4	70 (diam)		3	2
C5	660	440	5	4

side by side in a vacuum chamber which could be moved by a stepping motor in the direction perpendicular to the beam. Thus any of the two targets could be quickly brought into the momentum-recombination focus of the K3 line with a position reproducibility of better than 1 mm. The temperature of liquid hydrogen was controlled within ± 0.13 K. The resulting density variation of liquid hydrogen was $\pm 0.21\%$.

The beam was defined by trigger scintillation counters $C1$, $C2$, and $C3$, and was focused onto the target placed in the beam line. The characteristics of the trigger counters are summarized in Table III.

To detect annihilation events, about 95% of the solid angle around the target was covered by scintillation counters. Two walls of scintillation counters with a hole at the center sandwiched the target. Inside the vacuum chamber was installed another scintillation counter.[22] These were called annihilation counters. Detailed arrangement of the counters around the target is shown in Fig. 2.

The transmitted particles were detected by a circular transmission counter $C4$. Downstream of $C4$ were located a quadrupole doublet ($Q9$ and $Q10$) and a bending magnet ($D3$) which constituted the beam-monitoring spectrometer with solid-angle acceptance of 14 msr. The particles passed through this spectrometer were detected by a scintillation counter $C5$ and momentum-analyzed by a hodoscope $H3$ placed near the focal plane of the spectrometer. The hodoscope $H3$ consisted of 26 overlapping scintillators to form 51 horizontally divided channels. Between $Q10$ and $C5$, a helium bag was installed.

The magnetic fields of the bending magnet $D3$ were carefully measured by an NMR magnetometer as a function of the excitation current. The absolute values of the beam momenta were determined by this magnet to $\pm 0.5\%$, after having applied the correction for energy losses by the materials in the beam path. The event-by-event-basis momentum resolution of this spectrometer was not very good ($\pm 0.9\%$) because (i) the hodoscope $H3$ was not located exactly in the focal plane due to spatial limitation of the experimental area and (ii) the beam had a finite size at the experimental focus. Nevertheless, the relative momentum corresponding to the central orbit of each spectrometer setting was known with an accuracy of $\pm 0.05\%$ by analyzing a large number of data samples.

The trajectories of incoming and outgoing charged particles were measured by multiwire proportional chambers of dual-coordinate readout, MWPC1 and MWPC2, and

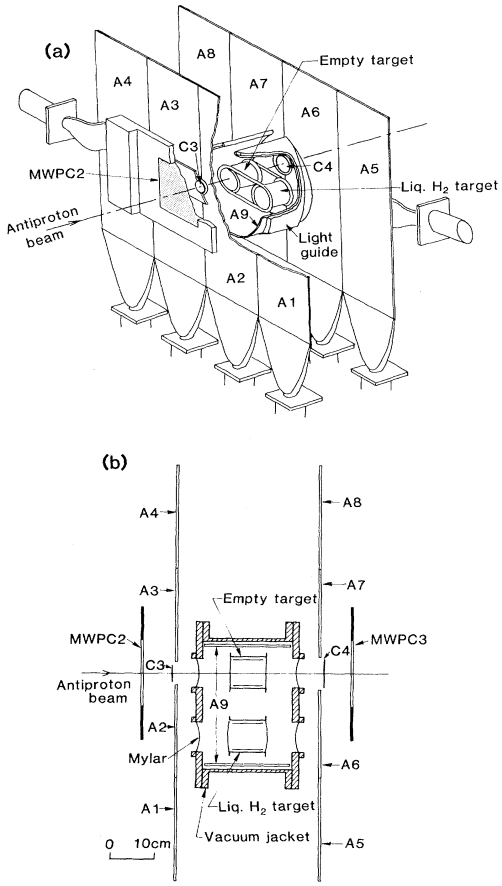

FIG. 2. Details of the apparatus around the experimental target. (a) Exploded view where the vacuum chamber for the liquid-hydrogen target is not shown. (b) Plan view. $A1$—$A9$ are the annihilation counters.

MWPC3—5, respectively. One coordinate of each MWPC was read out from a 2-mm-spacing anode-wire plane. The other coordinate was obtained by a cathode-coupled delay line technique. The hit coordinate along the cathode-coupled delay line was given by the propagation times of the induced signal injected to the delay line with a delay time of 160 nsec/cm. To cope with a high charged-particle rate, the electronics for time-to-digital conversion was capable of digitizing up to two signals arriving while the gate was open. The rms space resolution of the cathode readout was 0.45 mm. The efficiency of the cathode readout was dependent on the ionization loss and the rate of the charged particles. Consequently, the beam intensity was controlled to give a charged-particle rate of about 10^5 sec^{-1}, and the efficiency for the antiprotons was about 95% at 500 MeV/c, decreasing to 85% at 700 MeV/c.[23] Further details of the performance of these MWPC's have been described elsewhere.[24]

A hodoscope $H2$ located between $Q9$ and $Q10$ gave rough two-dimensional coordinates of the transmitted charged particles to help, if necessary, resolve ambiguities in orbit reconstruction using MWPC's 3—5.

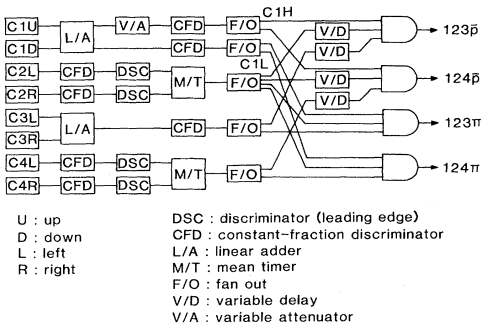

FIG. 3. Simplified block diagram of the fast trigger logic.

C. Electronics

The fast trigger logic was simply a threefold coincidence of the counters $C1$, $C2$, and $C3$ timed to the antiprotons. The block diagram of the fast trigger logic is shown in Fig. 3.

The timing of the coincidence $C1 \cdot C2 \cdot C3$ was sufficient to reject pions, except for the case that two pions traversed the counter $C1$ with such a time relation that the second pion signal from $C1$ and the first pion signals from $C2$ and $C3$ faked the antiproton timing. (Since the distance between the counters $C2$ and $C3$ was short, the twofold $C2 \cdot C3$ coincidence timing for antiprotons overlapped with that for pions.) Due to the high counting rate of $C1$, this kind of accidental trigger dominated when discriminator thresholds for the counters $C1$—$C3$ were set low enough to count minimum-ionizing particles.

To reduce the accidental trigger to a negligible level, we set the discriminator threshold for $C1$ high enough to reject minimum-ionizing particles. In fact, the analog signal from $C1$ was split: one was fed directly to a discriminator (whose output defined $C1_L$), and the other was attenuated and fed to another discriminator (whose output defined $C1_H$). The antiproton trigger was given by $C1_H \cdot C2 \cdot C3$. Residual contamination of the accidental triggers was eliminated in the off-line analysis (see Sec. III B).

Besides the antiproton trigger, we set up the pion trigger and both antiproton and pion triggers using $C1$, $C2$, and $C4$. To summarize, we had the following triggers:

$C1_H \cdot C2 \cdot C3$ timed to antiprotons($123\bar{p}$)

$C1_L \cdot C2 \cdot C3$ timed to pions(123π)

$C1_H \cdot C2 \cdot C4$ timed to antiprotons($124\bar{p}$)

$C1_L \cdot C2 \cdot C4$ timed to pions(124π) .

The 123π trigger was only used for calibration purposes such as the efficiency measurement of the MWPC's. The $124\bar{p}$ and 124π triggers were mainly used for the beam tuning.

The analog signals from $C1$—$C5$ were recorded in duplicate by independent LRS 2248 analog-to-digital converter (ADC) modules. This was motivated by the following reasons:

(i) The gate for the antiproton signal should be narrow

so as not to integrate other signals in addition, but the pion signal was also desired to be recorded.

(ii) Since the counters $C1$—$C5$ were important to identify antiprotons and pions, a fail-safe system was desired for pulse-height measurement. (In fact, LRS 2248 showed occasional malfunction, which will be discussed later in Sec. III C.) One ADC module was gated by a narrow (30 nsec) pulse timed to the antiproton signal and denoted as ADC^{N}. The other ADC module was gated by a 150-nsec pulse, wide enough to accept the pion signal, and denoted as ADC^{W}. In addition, the timing signals from $C1$—$C5$ were recorded by LRS 2226A timer-to-digital-converter (TDC) modules.

Data were collected and stored on a magnetic tape by a PDP-11/34 computer with a BDO-11 branch driver.

D. Experimental procedure

Data were taken at 27 spectrometer settings between 400 and 730 MeV/c. The measured momentum range was repeatedly swept as a check on reproducibility, in steps of one half of a beam-momentum bite of $\pm 2\%$. Thus there was no gap in the measured momentum range, and total cross section at any beam momentum was measured with two different spectrometer settings.

At each spectrometer setting, at least two independent sets of measurements with three to four full-empty cycles were made. In particular, we performed four or more independent sets of measurements between 435 and 617 MeV/c. Each time the spectrometer setting was changed, beam properties such as the intensity, $\pi^{-}/\bar{p}$ ratio, phase space, and momentum distribution were carefully checked prior to the measurement of total cross section.

The data collected by the on-line computer (PDP 11/34) were temporarily stored into memory. When the memory allocated for the data storage became full, its contents were dumped onto a magnetic tape as well as transferred to a KEK central computer, HITAC 8800, via a computer network KEKNET[25] for real-time analysis.

A total of 1.5×10^{7} events was recorded and analyzed. About $\frac{2}{3}$ of the recorded events was taken with the target full and the rest of the events was taken with the target empty.

III. DATA ANALYSIS

A. Description of the method

Here we first formulate the principle of our total-cross-section measurement, and then describe an overview of the data reduction.

The differential cross section of $\bar{p}p$ elastic scattering is given by

$$\frac{d\sigma}{dt}=|f_C(t)+f_N(t)|^2 , \tag{1}$$

where $-t$ is the four-momentum transfer, $f_C(t)$ is the Coulomb amplitude, and $f_N(t)$ is the nuclear-elastic amplitude. Defining

$$\frac{d\sigma_C}{dt}\equiv |f_C|^2 , \tag{2}$$

$$\frac{d\sigma_I}{dt}\equiv 2\mathrm{Re}(f_N^{*}f_C) , \tag{3}$$

$$\frac{d\sigma_N}{dt}\equiv |f_N|^2 , \tag{4}$$

Eq. (1) is written as

$$\frac{d\sigma}{dt}=\frac{d\sigma_C}{dt}+\frac{d\sigma_I}{dt}+\frac{d\sigma_N}{dt} , \tag{5}$$

where $d\sigma_C/dt$, $d\sigma_I/dt$, and $d\sigma_N/dt$ represent the purely Coulomb, Coulomb-nuclear-interference, and nuclear contributions to the differential cross section of elastic scattering, respectively.

The Coulomb amplitude is given by

$$f_C(t)=\frac{2\sqrt{\pi}\hbar c\alpha}{\beta t}F(t)\exp[-i\delta(t)] , \tag{6}$$

where α is the fine-structure constant, β the laboratory velocity of the incident $\bar{p}$, $\delta(t)$ the Coulomb phase[26]

$$\delta(t)=-[\ln(R^2t)+0.5772]\alpha/\beta \tag{7}$$

with $R^2=9.5\ \mathrm{GeV}^{-2}$, and $F(t)$ the Coulomb form factor:

$$F(t)=G^2(t)=(1+t/0.71)^{-4} , \tag{8}$$

where $G(t)$ is the electromagnetic form factor of the proton.

For small t, the differential cross section of elastic scattering due to the nuclear interaction is assumed to be extrapolated from the diffraction region:

$$\frac{d\sigma_N}{dt}=\left[\frac{d\sigma_N}{dt}\right]_{t=0}\exp(-bt) , \tag{9}$$

where b is the slope parameter. With use of the optical theorem, the nuclear-elastic amplitude is written as[27]

$$\begin{aligned} f_N(t)&=\mathrm{Im}f(0)(\rho+i)\exp(-\tfrac{1}{2}bt)\\ &=\frac{\sigma_{\mathrm{tot}}}{4\sqrt{\pi}\hbar c}(\rho+i)\exp(-\tfrac{1}{2}bt) , \end{aligned} \tag{10}$$

where σ_{tot} is the total cross section and ρ is the real-to-imaginary ratio of the forward elastic amplitude which is assumed to be constant for small t ($\lesssim 0.01$).

Substituting Eqs. (6) and (10), Eqs. (2)—(4) are given as

$$\frac{d\sigma_C}{dt}=4\pi\left[\frac{\alpha\hbar c}{\beta t}\right]^2F^2(t) , \tag{11}$$

$$\frac{d\sigma_I}{dt}=\frac{\alpha\sigma_{\mathrm{tot}}}{\beta t}F(t)\exp(-\tfrac{1}{2}bt)(\rho\cos\delta-\sin\delta) , \tag{12}$$

$$\frac{d\sigma_N}{dt}=\left[\frac{\sigma_{\mathrm{tot}}}{4\sqrt{\pi}\hbar c}\right]^2(1+\rho^2)\exp(-bt) . \tag{13}$$

Before describing the principle of our total-cross-section measurement, let us consider the conventional transmission method. The partial cross section defined by a transmission counter is related to the probability that no charged particle is detected by that counter. Thus, the

partial cross section σ_i for the ith transmission counter subtending a solid angle of Ω_i with respect to the target is given by

$$\sigma_i=\int_{\Omega_i}^{4\pi}\left[\frac{d\sigma_C}{d\Omega}+\frac{d\sigma_I}{d\Omega}+\frac{d\sigma_N}{d\Omega}\right]d\Omega+\epsilon(\Omega_i)\sigma_{\text{inel}}\ , \tag{14}$$

where σ_{inel} is the total inelastic cross section, $\epsilon(\Omega_i)$ represents the probability that no charged particle hit the ith counter in all inelastic reactions, and $d\sigma/d\Omega$ is related to $d\sigma/dt$ as

$$\frac{d\sigma}{dt}=\frac{\pi}{p^{*2}}\frac{d\Omega}{d\Omega^*}\frac{d\sigma}{d\Omega}\ , \tag{15}$$

where the momentum p^* and solid angle Ω^* are defined in the center-of-mass frame. Since the total cross section is given by

$$\sigma_{\text{tot}}=\int_0^{4\pi}\frac{d\sigma_N}{d\Omega}d\Omega+\sigma_{\text{inel}}\ , \tag{16}$$

Eq. (14) is rewritten as

$$\sigma_i=\sigma_{\text{tot}}+\int_{\Omega_i}^{4\pi}\left[\frac{d\sigma_C}{d\Omega}+\frac{d\sigma_I}{d\Omega}\right]d\Omega-\int_0^{\Omega_i}\frac{d\sigma_N}{d\Omega}d\Omega$$

$$-[1-\epsilon(\Omega_i)]\sigma_{\text{inel}}\ . \tag{17}$$

The extrapolation of σ_i to zero solid angle ensures $\epsilon(\Omega_i)\to 1$ and $\int_0^{\Omega_i}(d\sigma_N/d\Omega)d\Omega\to 0$, and gives σ_{tot} provided that the second term on the right-hand side of Eq. (17) is calculated using Eqs. (11) and (12) and subtracted from σ_i.

In contrast to the conventional transmission method, we had only one transmission counter $C4$. It is then necessary to identify and reject the $C4$ hit due to inelastic reactions, and the partial cross section defined by $C4$ is given by

$$\sigma_{C4}=\sigma_{\text{tot}}+\int_{\Omega_{C4}}^{4\pi}\left[\frac{d\sigma_C}{d\Omega}+\frac{d\sigma_I}{d\Omega}\right]d\Omega$$

$$-\int_0^{\Omega_{C4}}\frac{d\sigma_N}{d\Omega}d\Omega\ , \tag{18}$$

where Ω_{C4} is the solid angle subtended by $C4$. In reality, both target and beam have finite sizes. Therefore we define the acceptance function $F_{C4}(\Omega)$ of $C4$, $0\le F_{C4}(\Omega)\le 1$, and write σ_{C4} as

$$\sigma_{C4}=\sigma_{\text{tot}}+\int_0^{4\pi}\left[\frac{d\sigma_C}{d\Omega}+\frac{d\sigma_I}{d\Omega}\right][1-F_{C4}(\Omega)]d\Omega$$

$$-\int_0^{4\pi}\frac{d\sigma_N}{d\Omega}F_{C4}(\Omega)d\Omega\ . \tag{19}$$

Since the second and the third terms on the right-hand side of this equation are calculable using Eqs. (11)–(13), the total cross section is obtained from σ_{C4}.[28] Figure 4 shows the acceptance function $F_{C4}(\theta)$ calculated by using the measured beam phase space, where θ is the scattering angle.

The total-cross-section measurement essentially consists in counting the number of the beam particles (N^B) and the number of the transmitted particles (N^T) with and without the liquid-hydrogen target. Representing the measurements with the full target and empty target by subscripts f and e, respectively, we have the relations

$$N_f^T=N_f^B\eta_1\eta_2\exp(-n\sigma_{C4})\ , \tag{20}$$

$$N_e^T=N_e^B\eta_1\eta_2\ , \tag{21}$$

where η_1 and η_2 represent the beam absorption by the nontarget materials before and behind the liquid-hydrogen target, respectively, and n is the number of target protons per cm^2. From Eqs. (20) and (21), σ_{C4} is given as

$$\sigma_{C4}=\frac{1}{n}\left[\ln\frac{N_f^B}{N_f^T}-\ln\frac{N_e^B}{N_e^T}\right]\ . \tag{22}$$

To determine N^B and N^T, we require (i) identification of the beam antiprotons and (ii) identification of the transmitted antiprotons using the counter data. Since the highest beam momentum in the present experiment is below the threshold for pion production, the requirement (ii) is sufficient to reject the events due to the inelastic reactions.

Finally we make comments on the differences between the present and previous analyses. In addition to the above requirements, we previously imposed the beam-phase-space cut and reconstruction of the transmitted-antiproton trajectory.

The beam-phase-space cut was imposed to guarantee that the beam particle indeed passed through the target. This cut, however, required that the hit coordinate be uniquely determined in both anode and cathode planes of MWPC1 and MWPC2, and caused about a 50% loss of events. Furthermore, part of the annihilation events was lost due to this cut, because annihilation products often caused multihits in MWPC1 and MWPC2. Thus it was necessary to correct for this bias.[29] Later we further investigated the properties of the K3 beam, and found that the beam was satisfactorily focused on the target and that the requirement of the beam-phase-space cut was safely

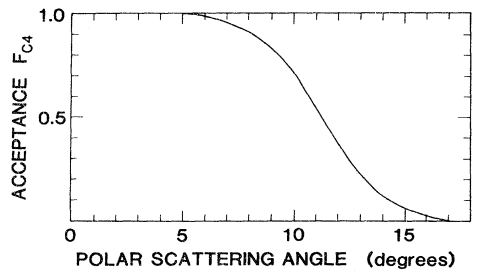

FIG. 4. The acceptance function F_{C4} as a function of the polar scattering angle θ.

dropped. Figure 5, for example, shows a distribution of the beam antiprotons at the center of the target at 500 MeV/c. It should be noted that there were some antiprotons elastically scattered by the counter $C3$, which were distributed near the wall of the target container. However, this effect is common to both full and empty targets and therefore cancels out in Eq. (22).

Reconstruction of the outgoing trajectory was previously required to define the solid-angle acceptance for the transmitted antiprotons so that the correction for nuclear elastic scattering was not very large. However, because of this requirement the counter $C4$ served as an absorbing material to increase the nontarget contribution. This fact as well as the statistical fluctuation of the reconstruction efficiency for the outgoing trajectories degraded the statistical accuracy of the resulted total cross section.

Even though the correction for nuclear elastic scattering is large due to the large solid-angle acceptance of $C4$, the statistical error of the total cross section is much improved in the present analysis, because the requirements of the beam-phase-space cut and the reconstruction of the outgoing trajectory have been dropped.

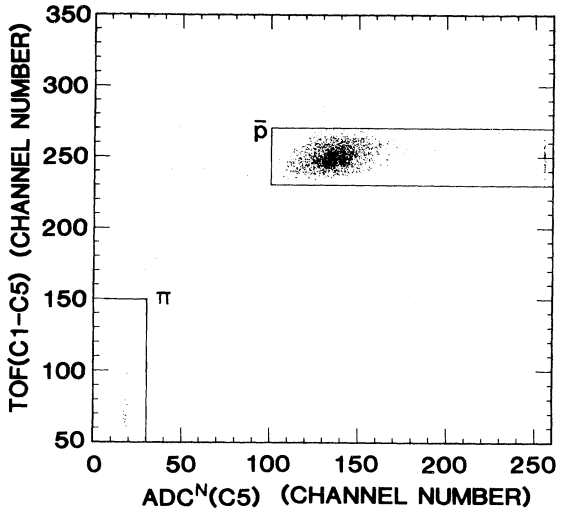

FIG. 6. Scatter plot of $ADC^N(C5)$ versus $TOF(C1-C5)$. The cuts indicated as $\bar{p}$ and π are used to select pure $\bar{p}$ and π samples.

B. Selection of incident-antiproton events

The events recorded on magnetic tapes included accidentally triggered events described in Sec. II C. The beam particles for this category of events were pions. Therefore, it was necessary to identify and reject the incident-beam pions. This was done by using the pulse-height and TOF information from the trigger counters, as follows.

(i) First, pure samples of beam antiprotons and beam pions were selected by using a two-dimensional scatter plot $ADC^N(C5)$ versus $TOF(C1-C5)$. Figure 6 shows an example. Here, the pion signals were out of timing of the gate for ADC^N, and appeared at the pedestal position of $ADC^N(C5)$.

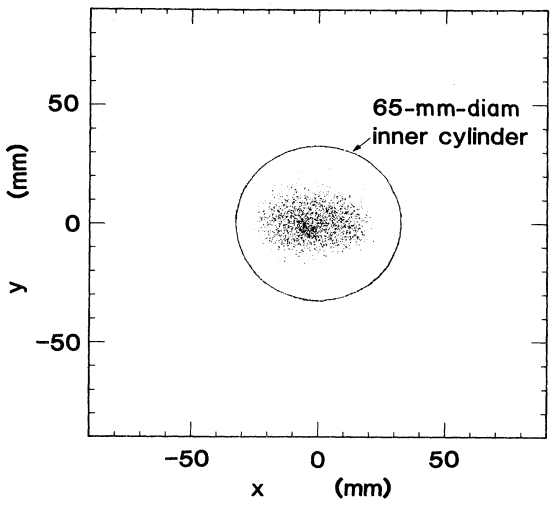

FIG. 5. Scatter plot of the projected horizontal (x) versus vertical (y) positions of the antiproton beam at the center of the liquid-hydrogen target. The circle indicates the position of the thin aluminum inner cylinder of the target container.

(ii) Second, the pulse-height and TOF distributions of the trigger counters corresponding to the pure antiproton and pion samples were examined and the cuts were determined. For example, Fig. 7 shows two-dimensional scatter plots $ADC^N(C3)$ versus $TOF(C1-C3)$ (a) for all events, (b) for the antiprotons, and (c) for the pions selected on the basis of the plot $ADC^N(C5)$ versus $TOF(C1-C5)$. Similarly, other one- and two-dimensional distributions constructed from the pulse-height and TOF information of the trigger counters were examined for pure beam-antiproton and beam-pion samples.

(iii) Cuts on these distributions were so determined as to reject beam pions to a level of 0.03% of the events surviving the cuts.

The residual contamination of the beam pions could be checked by examining the $ADC^N(C5)$ versus $TOF(C1-C5)$ plot for the events surviving the cuts. An example of the applied cuts is shown in Fig. 7(a).

With increase of the beam momentum, the separation of the beam pions and beam antiprotons became less clean, and tighter cuts were needed to maintain the required 0.03% level of pion contamination. As a result of these cuts, 1% to 8% of the incident-antiproton events were discarded depending on the beam momentum.

The incident-antiproton events selected by these cuts were written on other magnetic tapes with a condensed data format, if the beam momentum could be uniquely determined by the hit address of the hodoscope $H1$. About 10% of events were discarded due to no hit or multihit of $H1$. These magnetic tapes were called condensed tapes. About 1.3×10^7 events were stored in the condensed tapes, and were subjected to further analysis.

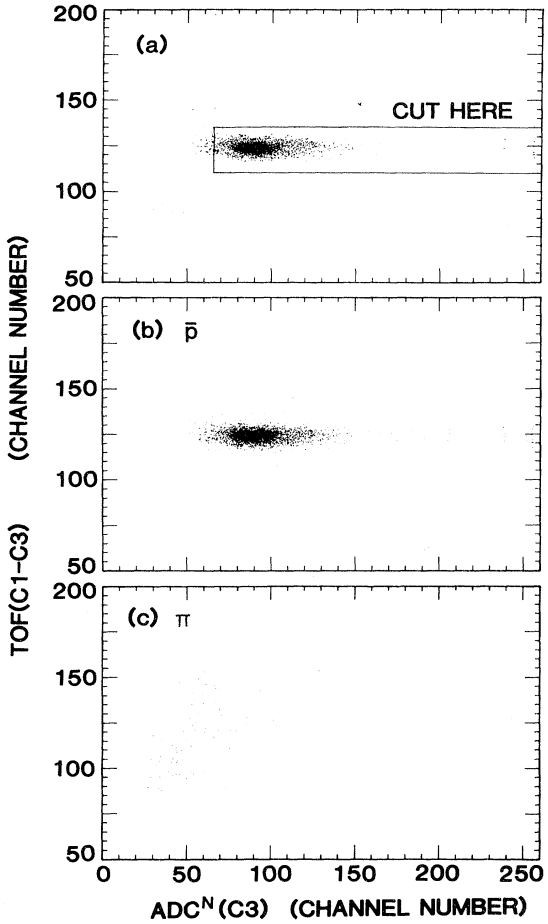

FIG. 7. Scatter plots of $ADC^N(C3)$ versus $TOF(C1-C3)$ for (a) all events, (b) pure $\bar{p}$ samples, and (c) pure π samples. The cut shown in (a) was applied to the data in order to purify the beam $\bar{p}$'s.

C. Identification of the transmitted antiprotons

If a charged-particle hit was recorded by the counter $C4$, it is necessary to determine whether that particle came from the inelastic reactions or not. The data from counters $C4$ and $C5$ and the hit multiplicity of the annihilation counters were used for this purpose. In the $\bar{p}p$ interactions below one-pion-production threshold, the antiproton cannot emerge from the inelastic reactions. Therefore it is sufficient to reject the inelastic reactions if the antiprotons are identified using the data from $C4$ and $C5$. The hit multiplicity of the annihilation counters was further used to strictly reject the annihilation events.

About 94% of the transmitted antiprotons reached $C5$ (at $\sim$500 MeV/c), and were unambiguously identified. The rest of the transmitted antiprotons were identified based on a two-dimensional plot of $ADC^N(C4)$ versus $ADC^W(C4)$. Since counter $C4$ was near the target, timing information $TOF(C1-C4)$ cannot be used to distinguish the antiprotons from the pions coming from the annihilation in the target. Figure 8(a) shows an example of the $ADC^N(C4)$ versus $ADC^W(C4)$ plot. Figure 8(b) is the same plot for the antiprotons identified by $C5$. It is seen that some events are scattered outside the correlated band for the antiprotons. Most of the events distributed above the antiproton band were caused by a hit of an additional charged particle while the ADC^W gate was open, but the events distributed below, and on both sides of the antiproton band were caused by a lost or added bit of the ADC's. It was found that an LRS 2248 ADC module exhibited this kind of malfunction for 0.6% of the triggered events. Since we had two independent ADC modules to record in duplicate the outputs of $C1-C5$, the chance for simultaneous malfunction of both ADC modules was negligible.

Since the rejction of the inelastic events should be done as completely as possible, the identification criteria for these events were stringently determined. This caused a

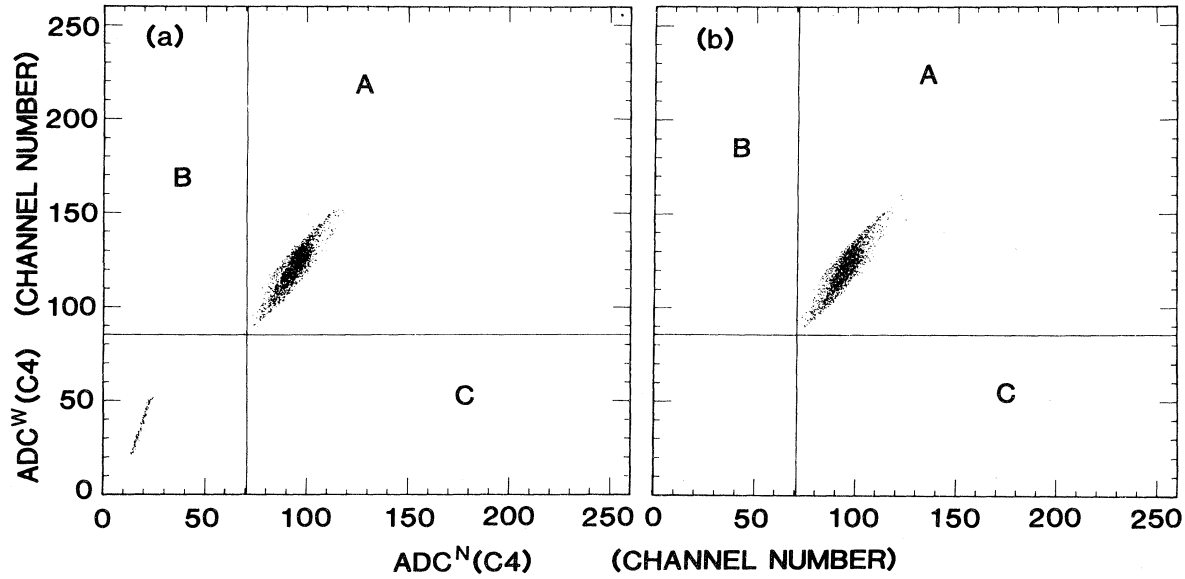

FIG. 8. Scatter plots of $ADC^N(C4)$ versus $ADC^W(C4)$ for (a) all events and (b) identified $\bar{p}$'s.

slight loss of transmitted antiprotons, but this is an effect which cancels in the full-empty subtraction, Eq. (22). The region A in Fig. 8 is predominantly occupied by antiprotons. However, slow and highly ionizing pions emerging from the annihilation reactions also exist in this region. These events were mostly found to have a high hit multiplicity (≥ 3) of the annihilation counters (see Fig. 9), and this condition was adopted to reject the inelastic events in the region A. In the regions B and C in Fig. 8, on the other hand, the condition for reliable rejection of the inelastic events was chosen to be at least one hit in the annihilation counters.

D. Corrections

The partial cross section σ_{C4} is deduced based on Eqs. (20)—(22). Here it is implicitly assumed that the values of $\eta_1\eta_2$ in both Eqs. (20) and (21) are the same. This is not true, however. Both η_1 and η_2 depend on the antiproton momentum. Since the incident beam momentum is common to the full- and empty-target runs, the value of η_1 in Eq. (20) is the same as that in Eq. (21). However, due to the momentum loss in liquid hydrogen, the antiproton having passed through the liquid-hydrogen target has a smaller momentum than that having passed through the empty target. Hence the value of η_2 in Eq. (20) is different from that in Eq. (21).

The correction to account for this difference was made as follows. The quantity $\ln(N_e^B/N_e^T)$ as a function of the incident beam momentum p was fitted to a polynomial of p^{-1}, $f(p)$. The correction factor $\Delta\sigma_{C4}$ is then given as

$$\Delta\sigma_{C4}=\frac{1}{n}[f(p)-f(p-\tfrac{1}{2}\Delta p)]\ , \tag{23}$$

where Δp is the momentum loss of the beam antiproton due to the liquid-hydrogen target. The correction factor $\Delta\sigma_{C4}$ is a smooth function of p. The uncertainty in the correction was not more than $\pm 5\%$ of $\Delta\sigma_{C4}$.

The corrections for Coulomb, Coulomb-nuclear-interference, and nuclear-elastic contributions were calculated using Eqs. (11)—(13) and Eq. (19). For these corrections, $\sigma_{\rm tot}$, ρ, and b must be given. For $\sigma_{\rm tot}$, we fitted the existing total cross section data[3,4,6,8] to a functional form $\sigma_{\rm tot}=A+B/p$, and obtained $A=61.2$ mb and $B=53.4$ mb GeV/c. Although these parameter values are slightly different from those determined from our own total cross section data, as given later in Sec. IV, we used this "world average" total cross section for calculating the correction factors in view of the fact that the ambiguity in $\sigma_{\rm tot}$ only resulted in a small error of the correction factors compared to the total systematic error. For the real-to-imaginary ratio ρ, we used the expression $\rho=p-0.45$

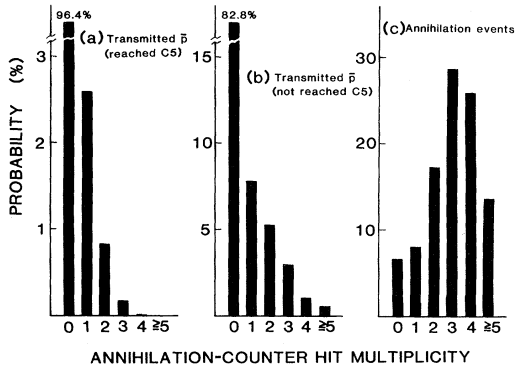

FIG. 9. Hit-multiplicity distributions of the annihilation counters. (a) For $\bar{p}$'s transmitted to $C5$. This represents the accidental hit of the annihilation counters. (b) For $\bar{p}$'s identified by $C4$, but not reached $C5$. These $\bar{p}$'s annihilated in $C4$ or somewhere between $C4$ and $C5$. (c) For $\bar{p}$'s annihilated in the liquid-hydrogen target.

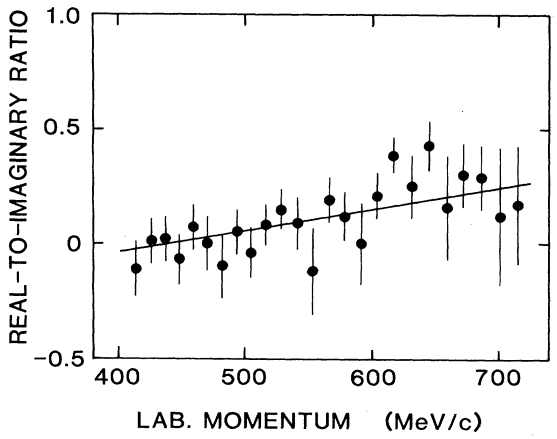

FIG. 10. The real-to-imaginary ratio ρ of the $\bar{p}p$ forward elastic amplitude (Ref. 20) concurrently determined with total cross section presented in this paper. The solid line shows the relation $\rho=p$ (GeV/c)-0.45.

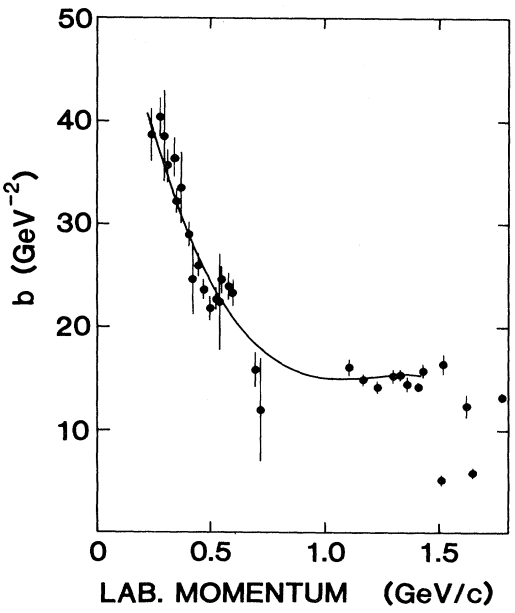

FIG. 11. The slope parameter b of $\bar{p}p$ forward scattering as a function of the beam momentum p. The solid curve shows the relation $b=65.62-129.4p+109.0p^2-30.19p^3$.

(where p is in GeV/c) on the basis of our own data obtained in this experiment,[30] which are shown in Fig. 10. Finally for the slope parameter b, we used the expression $b=65.62-129.4p+109.0p^2-30.19p^3$ which fits the existing data[31] as shown in Fig. 11. In calculating the correction factor for nuclear-elastic scattering, the absorption of the elastically scattered antiprotons by the liquid hydrogen was taken into account.

We note that all these correction factors are smooth functions of p. The Coulomb correction is very small due to the large acceptance of $C4$, and its ambiguity is negligible. To estimate the error in the correction for the Coulomb-nuclear interference, we calculated the correction factor by changing ρ by its uncertainty of ± 0.1. The resulted error for this correction is smoothly changing from ± 0.6 mb at 400 MeV/c to ± 0.2 mb at 700 MeV/c. The correction for nuclear-elastic scattering amounts to more than 10 mb owing to the large acceptance of $C4$. The error associated with this correction is mostly due to the systematic error in the calculation of the acceptance function $F_{C4}(\Omega)$. We estimate that the correction factor for nuclear-elastic scattering is calculated with $\pm 10\%$ of error.

E. Systematic errors

We consider the following systematic errors.

(i) The effective length of the liquid-hydrogen target was estimated to be 86.1 ± 0.7 mm at 20.4 K from the length along the cylinder axis at liquid-hydrogen temperature (86.5 mm), the shape of the Mylar end caps, and the observed beam phase space. Therefore the normalization error related to the target is $\pm 0.8\%$.

(ii) The systematic error caused by $\pm 0.5\%$ of uncertainty in the absolute beam momentum is given by $\Delta\sigma_{\rm tot}=(B/p)(\Delta p/p)=\pm 0.005\ B/p$, if the total cross section is expressed as $\sigma_{\rm tot}=A+B/p$. It changes smoothly from ± 0.7 mb at 400 MeV/c to ± 0.4 mb at 700 MeV/c.

(iii) The systematic errors caused by the residual pion contamination in the beam and by the loss of the transmitted antiprotons due to the hit-multiplicity criteria of the annihilation counters are estimated to be of order 0.1 mb. Note that these effects almost cancel in the full-empty subtraction. Only the statistical fluctuation of the pion contamination or loss of the transmitted antiprotons causes errors.

(iv) The systematic errors due to the failure in the rejection of inelastic events are estimated to be negligibly small. For example, if an antineutron from the charge-exchange process annihilates in the counter $C4$, it will be misidentified as a transmitted antiproton. From the forward differential cross section of $\bar{p}p\to\bar{n}n$ (~ 3 mb/sr),[32] the solid-angle acceptance of $C4$ (~ 0.15 sr), and the annihilation probability of the antineutron in the counter $C4$ ($\sim 2\%$), the error caused by this is less than 0.01 mb.

F. Mass resolution for the $\bar{p}p$ system

The mass resolution for the $\bar{p}p$ system is determined by the momentum spread of the beam and the energy loss of the antiproton in the liquid-hydrogen target. The solid curve in Fig. 12 shows the calculated mass resolution for the momentum spread of $\Delta p/p=2\%$ [full width at half maximum (FWHM)] determined by the hodoscope $H1$. Here the actual momentum resolution of $H1$ is taken into account. The dashed curve in Fig. 12 corresponds to the momentum spread of $\Delta p/p=1\%$. At low momenta, the mass resolution for the $\bar{p}p$ system is clearly dominated by the energy loss in the liquid-hydrogen target.

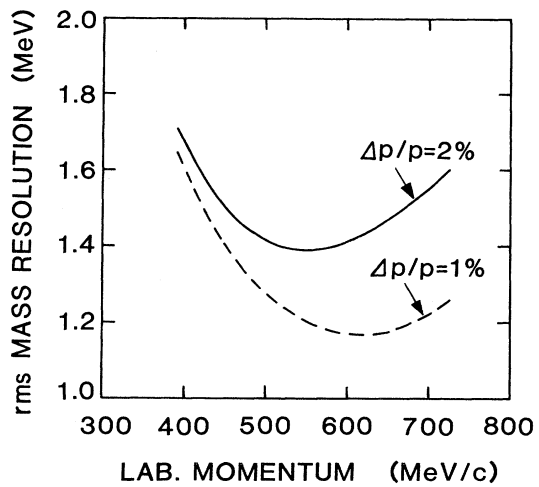

FIG. 12. The rms mass resolution for the $\bar{p}p$ system is shown for two binning methods of the beam momentum, $\Delta p/p=1\%$ (dashed curve) and 2% (solid curve).

Considering the mass resolution as well as the statistical accuracy, we adopted a bin width of $\Delta p/p=2\%$ for presentation of the data.

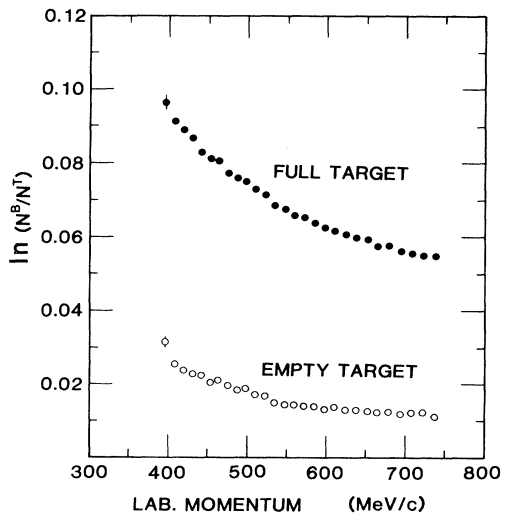

FIG. 13. The quantity $\ln(N^B/N^T)$ in Eq. (22) is plotted against the beam momentum for the full target (filled circles) and for the empty target (open circles).

TABLE IV. Experimental results. $\Delta\sigma_{C4}$ is the correction to account for the momentum difference between the target-full and target-empty runs. $\Delta\sigma_C$ is the correction for the Coulomb scattering. $\Delta\sigma_I$ is the correction for the Coulomb-nuclear interference effect. $\Delta\sigma_N$ is the correction for the nuclear-elastic scattering.

p (MeV/c)	σ_{C4} (mb)	$\Delta\sigma_{C4}$ (mb)	$\Delta\sigma_C$ (mb)	$\Delta\sigma_I$ (mb)	$\Delta\sigma_N$ (mb)	σ_{tot} (mb)
395.9	178.2	−2.5	−0.3	0.5	11.1	187.0±7.1±1.9
407.9	180.5	−2.2	−0.3	0.4	11.3	189.7±2.5±1.9
418.9	179.0	−2.0	−0.2	0.3	11.4	188.5±1.8±2.0
430.1	175.6	−1.8	−0.2	0.2	11.5	185.3±1.7±2.0
441.5	166.3	−1.7	−0.2	0.1	11.7	176.2±1.6±2.0
452.9	166.8	−1.5	−0.2	0.1	11.9	177.1±1.5±2.0
463.2	164.0	−1.4	−0.2	0.0	12.0	174.4±1.6±2.0
475.4	158.6	−1.3	−0.1	0.0	12.2	169.4±1.6±2.0
487.1	158.4	−1.2	−0.1	−0.1	12.4	169.4±1.4±2.0
497.7	154.7	−1.1	−0.1	−0.1	12.6	166.0±1.3±2.0
509.9	153.4	−1.0	−0.1	−0.2	12.8	164.9±1.3±2.0
522.0	150.1	−0.9	−0.1	−0.2	13.0	161.9±1.3±2.0
534.2	146.8	−0.8	−0.1	−0.2	13.2	158.9±1.4±2.0
547.4	145.5	−0.7	−0.1	−0.3	13.4	157.8±1.5±2.0
559.2	141.0	−0.7	−0.1	−0.3	13.6	153.5±1.4±2.0
571.6	140.7	−0.6	−0.1	−0.3	13.8	153.5±1.4±2.0
584.8	137.2	−0.5	−0.1	−0.3	14.1	150.4±1.4±1.9
597.5	135.4	−0.5	−0.1	−0.4	14.3	148.7±1.4±1.9
610.1	131.4	−0.4	−0.1	−0.4	14.6	145.1±1.4±1.9
624.0	131.1	−0.4	−0.1	−0.4	14.8	145.0±1.6±1.9
637.7	129.1	−0.4	−0.0	−0.4	15.1	143.4±2.0±1.9
652.1	128.1	−0.3	−0.0	−0.4	15.4	142.8±2.2±1.9
664.2	123.9	−0.3	−0.0	−0.4	15.7	138.9±2.1±1.9
678.6	124.1	−0.3	−0.0	−0.4	16.0	139.4±2.0±2.0
694.0	121.8	−0.3	−0.0	−0.4	16.3	137.4±2.0±2.0
707.9	119.6	−0.3	−0.0	−0.4	16.7	135.6±2.0±2.0
722.6	117.8	−0.2	−0.0	−0.4	17.0	134.2±1.5±2.0
737.4	120.2	−0.2	−0.0	−0.4	17.4	137.0±1.8±2.1

IV. RESULTS AND DISCUSSION

Figure 13 shows the momentum dependence of $\ln(N_f^B/N_f^T)$ and $\ln(N_e^B/N_e^T)$ in Eq. (22). The beam transmission ratios N^T/N^B at 500 MeV/c were 92.77±0.04% and 98.15±0.04% for the target-full and target-empty runs, respectively. The partial cross section σ_{C4} was deduced using Eq. (22) with $n^{-1}=2745.7\pm22.0$ mb. Table IV lists σ_{C4}, the correction factors calculated according to the prescription given in Sec. III D, and the resulting total cross section σ_{tot}. The random point-to-point error of σ_{tot} is essentially given by the statistical error of σ_{C4}, which is quoted as the first error attached to σ_{tot} in Table IV. The ambiguities associated with the correction factors listed in Table IV are smooth functions of the beam momentum as noted in Sec. III D. Therefore they are added in quadrature with the systematic normalization error and the error due to the ambiguity in the absolute beam momentum, to give the total systematic error which again is a smooth function of the beam momentum and is listed in Table IV as the second error attached to σ_{tot}. Figure 14 shows σ_{tot} and σ_{C4}, where the error bars represent the statistical error.

Our results are compared in Fig. 15 with some of the previously reported total-cross-section data.[3,4,6,8,12] Before discussing the structures seen in these spectra, we

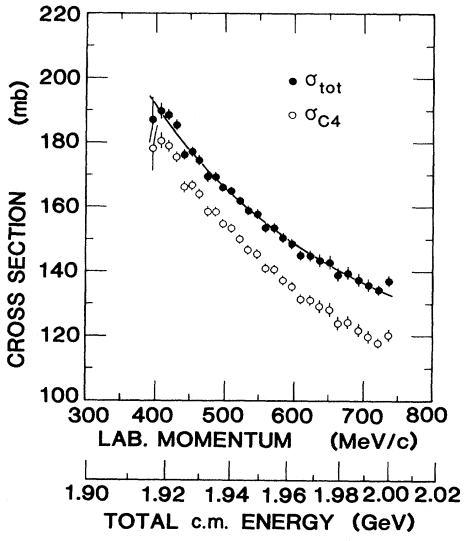

FIG. 14. The total cross section σ_{tot} and the partial cross section σ_{C4} are plotted against the beam momentum. The curve shows the result of the fit with $\sigma_{\text{tot}}=A+B/p$.

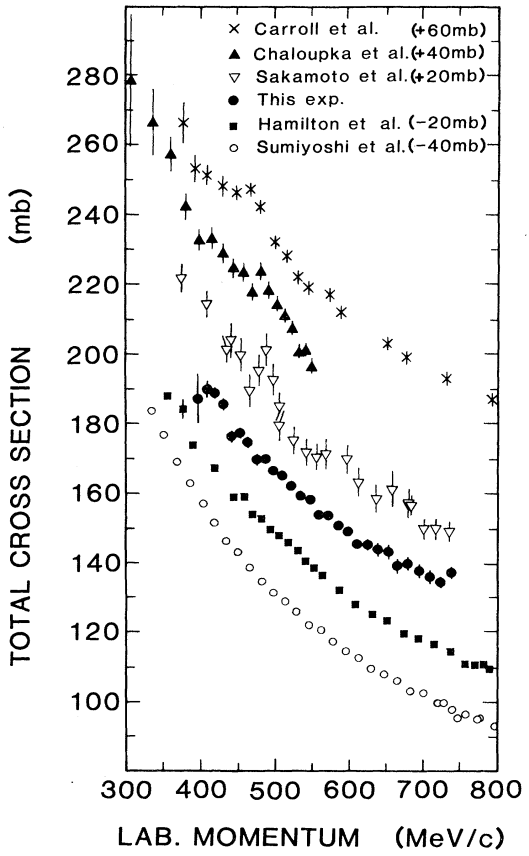

FIG. 15. Comparison of the $\bar{p}p$ total cross section data reported by several groups. For clarity, the data of Carroll *et al.* (Ref. 3) are shifted by +60 mb, those of Chaloupka *et al.* (Ref. 4) by +40 mb, those of Sakamoto *et al.* (Ref. 6) by +20 mb, those of Hamilton *et al.* (Ref. 8) by −20 mb, and those of Sumiyoshi *et al.* (Ref. 12) by −40 mb.

mention the following. Although the primary purpose of the present experiment is not to determine the absolute values of the total cross section very precisely, they are in reasonable agreement with high-statistics data of Hamilton *et al.*[8] and Sumiyoshi *et al.*[12] within the quoted normalization errors.

It is immediately seen that the data reported by Carroll *et al.*,[3] Chaloupka *et al.*,[4] and Sakamoto *et al.*[6] show significant, but mutually inconsistent structures around 500 MeV/c. However, there is no statistically significant structure in our data. The curve in Fig. 14 is the result of the fit with a well-known empirical formula $\sigma_{\rm tot}=A+B/p$, where we obtained $A=62.8$ mb and $B=51.6$ mb GeV/c with $\chi^2=23.2$. The deviation of the data points from the fitted curve is shown in Fig. 16 where the Breit-Wigner curves corresponding to the S-resonance parameters listed in Table I are shown for comparison. The mass resolution of the present experiment is taken into account in calculating these curves. The width of the S resonance corresponding to the data of Brückner *et al.*[5] was taken to be 4 MeV.

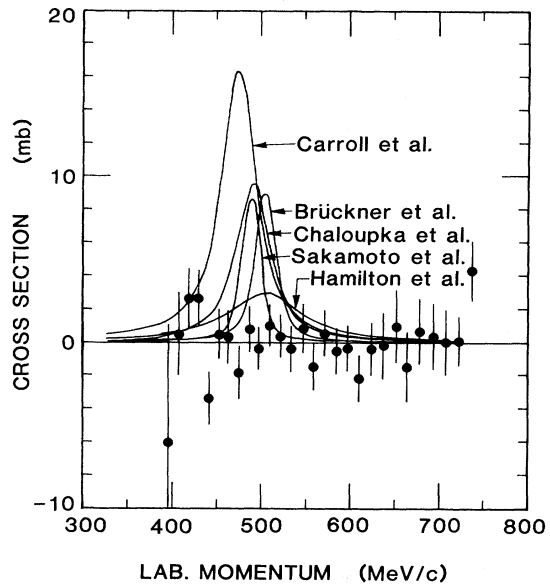

FIG. 16. The deviation of our total cross section data from the fitted curve of $\sigma_{\rm tot}=A+B/p$ is plotted against the beam momentum, and compared with the Breit-Wigner curves calculated by using the S-resonance parameters given by various groups.

In order to quantitatively test the existence of the S resonance, we fitted our data with a background plus a Breit-Wigner resonance of mass of M_R, width of Γ, and height of σ_R:

$$\sigma_{\rm tot}=A+B/p+\sigma_R/(1+\epsilon^2)\,, \tag{24}$$

where

$$\epsilon=2[M(p)-M_R]/\Gamma \tag{25}$$

with $M(p)$ being the mass of the $\bar{p}p$ system. The resonance parameters were taken from Table I, and therefore only A and B were free parameters in the fit. The mass resolution of the present experiment was folded into the theoretical curve, Eq. (24). The values of χ^2 obtained for various sets of the resonance parameters are given in Table V. This result indicates that the confidence levels

TABLE V. The χ^2 values obtained as a result of the fit with Eq. (24) using the S-resonance parameters taken from Table I. Note that the χ^2 value corresponding to the 90%-confidence-level upper limit for 26 degrees of freedom is 36.

S-resonance parameters taken from	χ^2
Carroll *et al.*	177.7
Chaloupka *et al.*	92.9
Brückner *et al.*	76.6
Sakamoto *et al.*	77.0
Hamilton *et al.*	30.3
No resonance ($\sigma_{\rm tot}=A+B/p$)	23.2

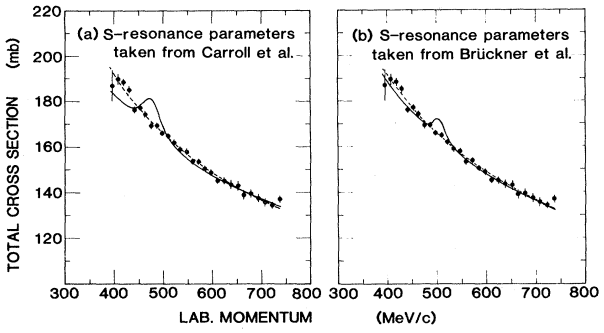

FIG. 17. The solid curves show the results of the fit to our total-cross-section data with the parametrization given by Eqs. (24) and (25). The S-resonance parameters are taken from (a) Carroll *et al.* (Ref. 3) and from (b) Brückner *et al.* (Refs. 5 and 18). The dashed curves show the result of the fit with $\sigma_{\text{tot}}=A+B/p$.

for the existence of the narrow S resonance reported by various groups are all less than 1%. However, the broad S resonance suggested by Hamilton *et al.*[8] is statistically not inconsistent with the present data. Figure 17 shows the results of the fits with the S-resonance parameters reported by (a) Carroll *et al.*[3] and by (b) Brückner *et al.*[5,18]

Finally we calculated 90%-confidence-level upper limits for resonance cross section (σ_R) allowed by our data for given mass (M_R) and width ($3 \leq \Gamma \leq 10$) parameters. The results are shown in Fig. 18. The 90%-confidence-level

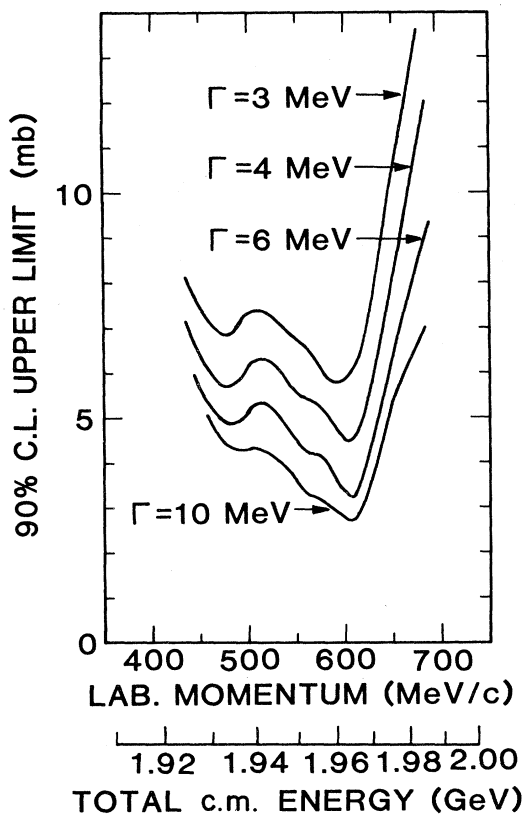

FIG. 18. 90%-confidence-level upper limits for σ_R of possible resonances as a function of mass and width.

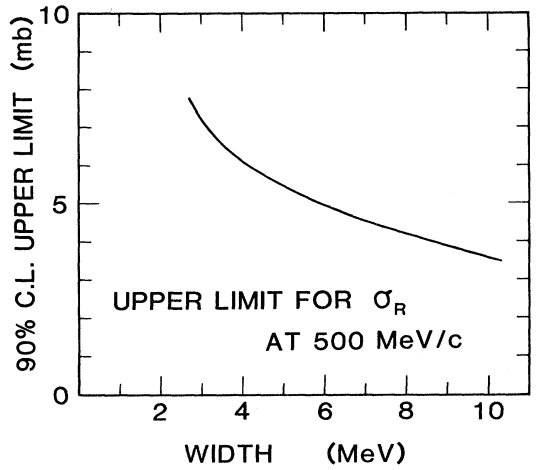

FIG. 19. 90%-confidence-level upper limits for σ_R of a possible resonance at 500 MeV/c as a function of width.

upper limits for a possible resonance around 500 MeV/c is also shown in Fig. 19 as a function of the width.

A direct comparison of our data with the structure observed in the $\bar{p}p$ annihilation cross section by Amsler *et al.*[17] ($\Gamma \sim 4$ MeV) is not possible, as the total resonance cross section is not given. However, if a baryonium is responsible for this structure, it must strongly couple to the elastic channel. The integrated annihilation cross section as read from a figure given in Ref. 17 is about 16 mb MeV. Assuming a simple Breit-Wigner resonance, if the total elastic cross section is more than 50% of the annihilation cross section, the total integrated cross section exceeds the 90%-confidence-level upper limit of 24 mb MeV set by the present result for $\Gamma \lesssim 4$ MeV.

V. CONCLUSIONS

We have presented $\bar{p}p$ total cross section between 395 and 740 MeV/c. The measurement was performed by the transmission method with use of a beam-monitoring spectrometer with a rms mass resolution for the $\bar{p}p$ system of 1.5 MeV in the S-resonance region. No statistically significant narrow structure was observed and the data were well represented by the form $\sigma_{\text{tot}}=A+B/p$. A 90%-confidence-level upper limit for Breit-Wigner resonances of width $\Gamma \lesssim 4$ MeV is 24 mb MeV at around 500 MeV/c. In particular, the narrow enhancements reported by Carroll *et al.*,[3] Chaloupka *et al.*,[4] Brückner *et al.*[5], and Sakamoto *et al.*[6] all exceed this limit.

ACKNOWLEDGMENTS

We would like to gratefully acknowledge the excellent machine operation of the staff of KEK accelerator department and the help of the staff of KEK experiment supporting group. We also wish to thank the KEK computer center where all stages of this analysis were done. This work was supported in part by a Grant in Aid from the Japanese Ministry of Education, Science, and Culture.

*Present address: National Laboratory for High Energy Physics, Oho, Ibaraki 305, Japan.

†Present address: Institute of Applied Physics, University of Tsukuba, Sakura, Ibaraki 305, Japan.

‡Present address: LICEPP, University of Tokyo, Tokyo 113, Japan.

[1]L. Montanet, Phys. Rep. 63, 201 (1980); T. Kamae, Nucl. Phys. A374, 25c (1982).

[2]B. Richter *et al.* [Phys. Lett. 126B, 284 (1983)] report the confirmation of some of the narrow peaks in the γ-ray spectrum from $\bar{p}p$ annihilation at rest observed by P. Pavlopoulos *et al.* [*ibid.* 72B, 415 (1978)]; F. Azooz *et al.* [*ibid.* 122B, 471 (1983)] report evidence for narrow $p\bar{n}$ and $\bar{p}n$ states of mass 2020 MeV produced in the $\bar{p}p$ interactions at the SLAC hybrid facility. A neutral state at 2020 MeV was previously reported by P. Benkheiri *et al.* [*ibid.* 68B, 483 (1977)]. See also Ref. 17.

[3]A. S. Carroll *et al.*, Phys. Rev. Lett. 32, 247 (1974).

[4]V. Chaloupka *et al.*, Phys. Lett. 61B, 487 (1976).

[5]W. Brückner *et al.*, Phys. Lett. 67B, 222 (1977).

[6]S. Sakamoto *et al.*, Nucl. Phys. B158, 410 (1979).

[7]M. Alston-Garnjost *et al.*, Phys. Rev. Lett. 35, 1685 (1975); R. P. Hamilton *et al.*, *ibid.* 44, 1179 (1980).

[8]R. P. Hamilton *et al.*, Phys. Rev. Lett. 44, 1182 (1980).

[9]T. Kamae, *et al.*, Phys. Rev. Lett. 44, 1439 (1980).

[10]E. Jastrzembski *et al.*, Phys. Rev. D 23, 2784 (1981).

[11]D. I. Lowenstein *et al.*, Phys. Rev. D 23, 2788 (1981).

[12]T. Sumiyoshi *et al.*, Phys. Rev. Lett. 49, 628 (1982).

[13]P. Allen *et al.*, in *Proceedings of the Fifth European Symposium on Nucleon Anti-Nucleon Interactions, Bressanone, Italy, 1980* (Institute Nazionale di Fisica Nucleare Sezione di Padova, Padova, 1980), p. 175.

[14]C. Daum *et al.*, Phys. Lett. 90B, 475 (1980).

[15]D. Aston *et al.*, Phys. Lett. 93B, 517 (1980).

[16]C. Daum *et al.*, Phys. Lett. 100B, 439 (1981).

[17]C. Amsler *et al.*, CERN Report No. CERN-EP/82-93, 1982 (unpublished).

[18]K. Kilian and B. Pietrzyk, in *Proceedings of the Seventh International Conference on High-Energy Physics and Nuclear Structure, Zürich, 1977,* edited by M. P. Locher (Birkhäuser, Basel, 1977), p. 85.

[19]H. Iwasaki *et al.*, Phys. Lett. 103B, 247 (1981).

[20]H. Iwasaki *et al.*, University of Tokyo Report No. UT-HE-83/13, 1983 (unpublished).

[21]T. Sumiyoshi *et al.*, Jpn. J. Appl. Phys. 22, 1606 (1983).

[22]H. Aihara *et al.*, Nucl. Instrum. Methods 184, 359 (1981).

[23]The dependence of the cathode-readout efficiency on the ionization loss and the charged-particle rate means that the reconstruction efficiencies of the incoming and outgoing trajectories are also dependent on these quantities. It should be noted, however, that the analysis presented in this paper does not use the trajectory reconstruction to deduce the total cross section.

[24]H. Iwasaki *et al.*, Jpn. J. Appl. Phys. 20, 189 (1981).

[25]Y. Asano *et al.*, Nucl. Instrum. Methods 159, 7 (1979).

[26]M. P. Locher, Nucl. Phys. B2, 525 (1967).

[27]We assume predominance of the spin-independent part of the $\bar{p}p$ forward amplitude.

[28]It is essentially important that $F_{C4}(\Omega)=1$ for $0 \leq \Omega \leq \Omega_0$ where Ω_0 is a not-too-small positive constant. Otherwise the second term on the right-hand side of Eq. (19) diverges if naively calculated, and the correction factors cannot be reliably calculated. If we try to use the counter *C*5 as a transmission counter, a difficult situation $F_{C5}(\Omega)\neq 1$ as $\Omega \rightarrow 0$ occurs because of multiple Coulomb scattering.

[29]In Ref. 9, the correction for this bias was quoted as the "backsplash" correction. There we did not make a great effort to obtain the absolute values of the total cross section. Later it was found that the backsplash correction was larger than that quoted in Ref. 9. As a result, the values of total cross section quoted in Ref. 9 are pushed up by about 10 mb. This mainly arose from the fact that the contribution to the backsplash correction from neutral particles (conversion of photons from π^0's and annihilation of antineutrons in the wall of the target vacuum chamber, etc.) was not taken into account.

[30]The values of ρ quoted in our preliminary report (Ref. 19) were deduced on the basis of σ_{tot} reported in Ref. 9. These values should be lowered by about 0.1 as a result of the increase of σ_{tot} presented in this paper. The corrected results for ρ are given in Ref. 20.

[31]P. Jenni *et al.*, Nucl. Phys. B94, 1 (1975); H. Kaseno *et al.*, Phys. Lett. 61B, 203 (1976); 68B, 487(E) (1977); J. E. Enstrom *et al.*, Particle Data Group, Lawrence Berkeley Laboratory Report No. LBL-58, 1972.

[32]A. Bettini *et al.*, in *Proceedings of the Fourth European Antiproton Symposium, Barr/Strasbourg, 1978,* edited by A. Fridman (Centre National de la Recherche Scientifique, Paris, 1979), Vol. I, p. 129; T. Tsuboyama *et al.*, Phys. Rev. D 28, 2135 (1983).